Unsupervised Image Classification using the Entropy/Alpha/Anisotropy Method in Radar Polarimetry

Shane R Cloude*, Eric Pottier**, Wolfgang M Boerner ***

*AEL Consultants, 26 Westfield Av., Cupar, Fife, KY15 5AA,Scotland, UK Tel/Fax: +44 (1334) 653958 e-mail: scloude@aelc.demon.co.uk, web-site: http://www.aelc.demon.co.uk

** Institut dŒlectronique et de T l communications de Rennes, UMR — CNRS, Universit de Rennes 1, P le Micro-Ondes Radar, Campus de Beaulieu — Bat. 11D, 35042 Rennes Cedex France
e-mail:eric.pottier@univ-rennes1.fr

***UIC-ECE Communications, Sensing & Navigation Laboratory 900 W. Taylor St., SEL (607) W-4210, M/C 154, CHICAGO IL/USA-60607-7018 T&F: +[1] (312) 996-5480
e-mail: boerner@ece.uic.edu

Abstract

In this paper we re-examine the entropy alpha approach to radar polarimetry and show how the basic method may be augmented by the addition of two new polarizing parameters, the propagation and helicity phase angles and three depolarizing parameters, the anisotropy A and two depolarizing eigenvector angles. We apply the technique to Polarimetric AIRSAR data for land, ice and forestry applications.

1. Introduction

In this paper we describe a method for unsupervised classification of polarimetric SAR imagery based on an eigenvector analysis of the coherency matrix. In previous publications [1,2,3], the entropy/alpha plane was introduced as a convenient means of displaying these eigenvector properties. It was further shown how, by using simple physical models, up to 8 important classes of terrain cover can be classified using this technique [1].

This method has also recently been used as a starting condition for a more sophisticated iterative classification method employing multi-variate Wishart statistics [5,6,7]. These studies have all highlighted the importance of optimising the number and diversity of classes to be used as input to the classifier. For this reason it is of interest to reconsider the details of the method and assess any possible extensions into new class types. Given the widespread availability of high quality calibrated POLSAR data and the imminent launch of space based polarimetric imaging radars, it is of timely interest to consider such an extension.

To do this, we first up-date the classification boundaries using recent developments in radar polarimetry [3,8,9] and interferometry [10,11,12] and then highlight the potential of using several new parameters for further refinements in the classification procedure. We concentrate on two new sets of polarimetric parameters, namely those arising from a polarising/depolarising decomposition of the coherency matrix [13]. The former are derived from the maximum eigenvector and offer two invariant phase angles, which so far have not been employed for classification. The latter arise from the depolarising subspace alone. One of these, the scattering anisotropy A, has already been suggested as a new feature to distinguish depolarising mechanisms in surface and volume scattering [3,5]. For example, A can be used to distinguish rough from smooth surfaces and to classify different types of vegetation cover. However, the depolarization subspace also offers two new parameters, which so far have not been fully exploited.

We first derive the key features of this classification method and then present some examples of its application to POLSAR data for land, sea ice and forestry applications.

2. Navigating the Entropy/Alpha Plane

The basic observable in radar polarimetry is the 2 x 2 complex scattering matrix [S]. For backscatter problems, the reciprocity theorem forces HV=VH and so this matrix is symmetric. When such SLC data is available then the coherency matrix can be directly derived by vectorising [S] into $\underline{k}$ using the Pauli spin matrices and then averaging products of the complex elements to generate a 3 x 3 positive semi-definite Hermitian matrix [T], as shown in equation 1.

However, often the user is provided not with SLC data but with multi-look Stokes matrix data [M]. It is important to realise that this format is entirely equivalent to the coherency matrix, although some care is required in transforming between matrices. The problem arises that, because of coding or measurement errors, small negative eigenvalues are obtained in converting from [M] to [T]. To cope with this case, matrix-filtering techniques have been developed [4].

In equation 1 we also show for reference the explicit mapping between the real symmetric Stokes matrix [M] and the coherency matrix [T]. Using this relationship [T] can be easily derived from Stokes matrix format data such as provided from the AIRSAR system.

$$[M]=\begin{bmatrix} m_1 & m_2 & m_3 & m_4 \\ m_2 & m_5 & m_6 & m_7 \\ m_3 & m_6 & m_8 & m_9 \\ m_4 & m_7 & m_9 & m_{10} \end{bmatrix} \Rightarrow$$

$$[T]=\frac{1}{2}\begin{bmatrix} \frac{1}{2}(m_1+m_5+m_8-m_{10}) & m_2-im_9 & m_3+im_7 \\ m_2+im_9 & \frac{1}{2}(m_1+m_5-m_8+m_{10}) & m_6+im_4 \\ m_3-im_7 & m_6-im_4 & \frac{1}{2}(m_1-m_5+m_8+m_{10}) \end{bmatrix} \qquad -1)$$

$$[T]=\begin{bmatrix} \left\langle |S_{hh}+S_{vv}|^2 \right\rangle & \left\langle (S_{hh}+S_{vv})(S_{hh}-S_{vv})^* \right\rangle & 2\left\langle (S_{hh}+S_{vv})S_{HV}^* \right\rangle \\ \left\langle (S_{hh}-S_{vv})(S_{hh}+S_{vv})^* \right\rangle & \left\langle |S_{hh}-S_{vv}|^2 \right\rangle & 2\left\langle (S_{hh}-S_{vv})S_{HV}^* \right\rangle \\ 2\left\langle (S_{hh}+S_{vv})^* S_{HV} \right\rangle & 2\left\langle (S_{hh}-S_{vv})^* S_{HV} \right\rangle & 4\left\langle |S_{hv}|^2 \right\rangle \end{bmatrix}=\begin{bmatrix} a & z_1 & z_2 \\ z_{1p} & b & z_3 \\ z_{zp} & z_{3p} & c \end{bmatrix}$$

If we write [T] in the explicit form shown in equation 1 then the 3 real non-negative eigenvalues of [T] can then be derived analytically as

$$\lambda_1 = \frac{2^{\frac{1}{3}} S_2}{3.S_3^{\frac{1}{3}}} + \frac{1}{3} Tr(T) + \frac{S_3^{\frac{1}{3}}}{3.2^{\frac{1}{3}}}$$

$$\lambda_2 = -\frac{(1+i\sqrt{3})S_2}{3.2^{\frac{2}{3}}.S_3^{\frac{1}{3}}} + \frac{1}{3} Tr(T) - \frac{(1-i\sqrt{3})S_3^{\frac{1}{3}}}{6.2^{\frac{1}{3}}} \qquad \text{- 2)}$$

$$\lambda_3 = -\frac{(1-i\sqrt{3})S_2}{3.2^{\frac{2}{3}}.S_3^{\frac{1}{3}}} + \frac{1}{3} Tr(T) - \frac{(1+i\sqrt{3})S_3^{\frac{1}{3}}}{6.2^{\frac{1}{3}}}$$

where Tr(T) = (a+b+c) and the secondary parameters S_2 and S_3 can be calculated from the following relationships

$$S_1 = ab + ac + bc - z_1 z_{1p} - z_2 z_{2p} - z_3 z_{3p}$$

$$S_2 = a^2 - ab + b^2 - ac - bc + c^2 + 3z_1 z_{1p} + 3z_2 z_{2p} + 3z_3 z_{3p}$$

$$\det(T) = abc - cz_1 z_{1p} - bz_2 z_{2p} + z_1 z_{2p} z_3 + z_{1p} z_2 z_{3p} - az_3 z_{3p} \qquad \text{- 3)}$$

$$S_3 = 27\det(T) - 9S_1 Tr(T) + 2Tr(T)^3 + \sqrt{\left(27\det(T) - 9S_1 Tr(T) + 2Tr(T)^3\right)^2 - 4S_2^3}$$

The eigenvectors of [T] can also be calculated as the columns of a 3 x 3 matrix $[U_3] = [\underline{e}_1\ \underline{e}_2\ \underline{e}_3]$ where

$$\underline{e}_i = \begin{bmatrix} \frac{\lambda_i - c}{z_{2p}} + \frac{((\lambda_i - c)z_{1p} + z_{2p} z_3) z_{3p}}{((b - \lambda_i) z_{2p} - z_{1p} z_{3p}) z_{2p}} \\ \frac{(\lambda_i - c) z_{1p} + z_{2p} z_3}{(b - \lambda_i) z_{2p} - z_{1p} z_{3p}} \\ 1 \end{bmatrix} \qquad \text{- 4)}$$

The coherency matrix [T] also has an associated Hermitian form $q_i \geq 0$, which can be used to generate the level of scattered power into mechanism $\underline{w}_i$ as [14]

$$q_i = \underline{w}^{*T} [T] \underline{w} \qquad \text{- 5)}$$

The eigenvalues of [T] therefore have direct physical significance in terms of the components of scattered power into a set of orthogonal unitary scattering mechanisms given by the eigenvectors of [T], which for radar backscatter themselves form the columns of a 3 x 3 unitary matrix. Hence we can write an arbitrary coherency matrix in the form

$$[T] = [U_3]\begin{bmatrix} \lambda_1 & 0 & 0 \\ 0 & \lambda_2 & 0 \\ 0 & 0 & \lambda_3 \end{bmatrix}[U_3]^{*T} \quad \lambda_1 \geq \lambda_2 \geq \lambda_3 \geq 0 \quad 0 \leq P_i = \frac{\lambda_i}{\sum \lambda} \leq 1 \tag{- 6)}$$

where the P_i may be interpreted as probabilities for a Bernoulli model of scattering from random media [1] as a weighted sum of coherent scattering mechanisms given by the 3 eigenvectors or columns of $[U_3]$ as shown in equation 7

$$[\mathrm{T}] = [\mathrm{U}_3]\begin{bmatrix} \lambda_1 & 0 & 0 \\ 0 & \lambda_2 & 0 \\ 0 & 0 & \lambda_3 \end{bmatrix}[\mathrm{U}_3]^{*T}$$
$$\Big\downarrow \tag{- 7)}$$
$$[U_3] = \begin{bmatrix} \cos\alpha_1 & \cos\alpha_2 & \cos\alpha_3 \\ \sin\alpha_1\cos\beta_1 e^{i\delta_1} & \sin\alpha_2\cos\beta_2 e^{i\delta_2} & \sin\alpha_3\cos\beta_3 e^{i\delta_3} \\ \sin\alpha_1 \sin\beta_1 e^{i\gamma_1} & \sin\alpha_2 \sin\beta_2 e^{i\gamma_2} & \sin\alpha_3 \sin\beta_3 e^{i\gamma_3} \end{bmatrix}$$

While the eigenvalues and eigenvectors are the primary variables of interest, several secondary parameters can be defined as functions of the components of the eigen-decomposition. There are four of these of interest in radar, two from the eigenvalues, namely the entropy and anisotropy, and two from the eigenvectors, the α and β angles, as shown in figure 1.

The parameters α and β can be interpreted as generalised rotations of the mechanism w as shown in figure 2. In fact the parameter β is just the physical orientation of the object about the line of sight. However, the α parameter is an indicator of the type of scattering and is called the scattering mechanism.

$$\left.\begin{aligned} & H = -P_1 \log_3 P_1 - P_2 \log_3 P_2 - P_3 \log_3 P_3 && 0 \leq \mathrm{H} \leq 1 \\ & \mathrm{A} = \frac{\mathrm{P}_2 - P_3}{P_2 + P_3} && 0 \leq \mathrm{A} \leq 1 \end{aligned}\right\} \text{Eigenvalue Parameters}$$

$$\left.\begin{aligned} & \overline{\alpha} = \mathrm{P}_1\alpha_1 + \mathrm{P}_2\alpha_2 + \mathrm{P}_3\alpha_3 \quad 0 \leq \overline{\alpha} \leq 90^o && \alpha_\mathrm{i} = \cos^{-1}\left(\frac{k_0}{|\underline{k}|}\right) \\ & \overline{\beta} = \beta_1 \qquad\qquad 0 \leq \overline{\beta} < 360^o && \beta_\mathrm{i} = \tfrac{1}{2}\tan^{-1}\left(\frac{2\,\mathrm{Re}(k_1 k_2^*)}{k_1 k_1^* - k_2 k_2^*}\right) \end{aligned}\right\} \text{Eigenvector Parameters}$$

Figure 1 : Secondary Scattering Parameters Derived from the Eigenvalues and Eigenvectors of [T]

If the pair H/α are plotted on a plane then they are confined to a finite zone as shown in figure 3. The alpha parameter ranges from 0 to 90 degrees and is an average representation of the eigenvector information while the entropy lies between 0 and 1 and represents the eigenvalue information in [T]. As both are invariant to the type of polarization base considered, they provide a convenient pictorial representation of the information in [T].

$$\underline{e}=\begin{bmatrix}1\\0\\0\end{bmatrix}=\begin{bmatrix}\cos\alpha & \sin\alpha & 0\\ -\sin\alpha & \cos\alpha & 0\\ 0 & 0 & 1\end{bmatrix}\begin{bmatrix}1 & 0 & 0\\ 0 & \cos\beta & \sin\beta\\ 0 & -\sin\beta & \cos\beta\end{bmatrix}\begin{bmatrix}e^{-i\phi_1} & 0 & 0\\ 0 & e^{-i\phi_2} & 0\\ 0 & 0 & e^{-i\phi_3}\end{bmatrix}\underline{w}$$

$$\underline{k}'=\begin{bmatrix}\cos\Delta\alpha & -\sin\Delta\alpha & 0\\ \sin\Delta\alpha & \cos\Delta\alpha & 0\\ 0 & 0 & 1\end{bmatrix}\underline{k} \qquad \underline{k}'=\begin{bmatrix}1 & 0 & 0\\ 0 & \cos\Delta\beta & -\sin\Delta\beta\\ 0 & \sin\Delta\beta & \cos\Delta\beta\end{bmatrix}\underline{k}$$

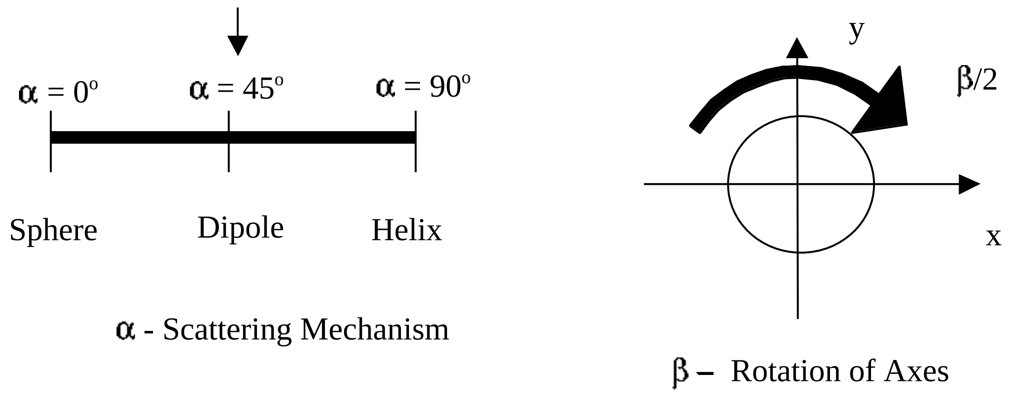

Figure 2 : The definition of the α and β parameters

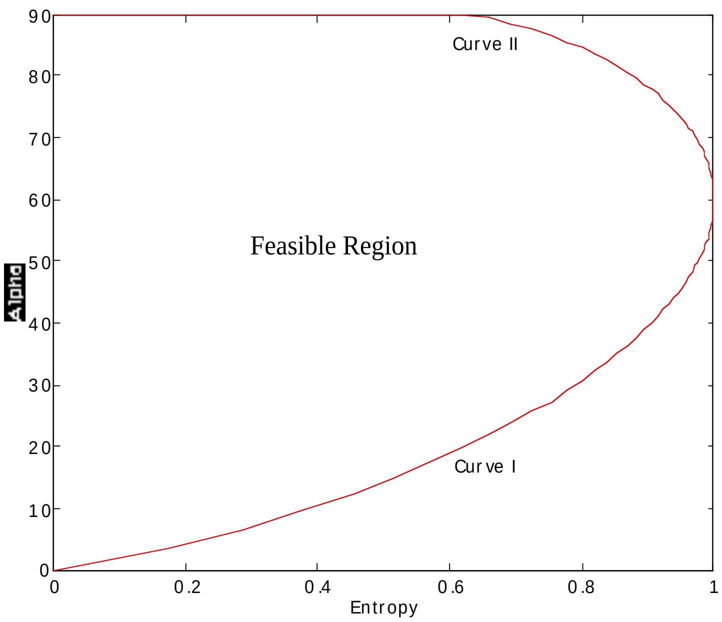

Figure 3 : The entropy/alpha plane

Note that because of the averaging across the eigenvectors, the visible range of α reduces with increasing entropy. The α variation is bounded as shown by curves I and II in figure 3. Curve I represents the lowest α value for a given entropy and is achieved in the case of azimuthal symmetry in the scattering volume. The maximum α curve II is achieved for multiple scattering in the volume. All random volume problems can be mapped as a point in this plane and hence this forms the basis for the unsupervised classification procedure to be described.

Figure 4 shows a set of four important mappings onto this plane as follows:

1) The first mapping is to segment the plane into single and multiple scattering by drawing the mean value of alpha as a function of entropy (shown as the black line in figure 4a). We see that at H = 0, α = 45 degrees is the mid-point and this corresponds to dipole scattering when one of the copolar scattering coefficients falls to zero. The phase change from single to multiple scattering occurs at this zero point. All points above this line correspond to multiple scattering while those below to single. This is the first important segmentation of the H/α plane.

2) The next key mapping is to consider volume scattering [8,9,15]. Here we make use of two key results: the first is that vegetation is a mixed ordered/stochastic scattering environment where the leafy structure provides a random background to the more ordered stalk and branch structure. A common model is to use a mixed uniaxial crystal plus random volume as shown in figure 5. For this reason we must include the possibility of both ends of the order spectrum in radar polarimetry i.e. situations where the uniaxial component is dominant and those where the random component is strongest.

   The second key result is that the scattering vector for a spheroidal particle in arbitrary orientation can be written in the factored form [8,16,22]

$$\underline{k} = \begin{bmatrix} 1 & 0 & 0 \\ 0 & \cos 2\theta & -\sin 2\theta \\ 0 & \sin 2\theta & \cos 2\theta \end{bmatrix} \begin{bmatrix} 2+(R-1)\cos^2\tau \\ (R-1)\cos^2\tau \\ 0 \end{bmatrix} \qquad \text{- 8)}$$

   where the parameters are defined as follows:

   θ - particle canting angle $0 \le \theta < 2\pi$
   τ - particle tilt angle $0 \le \tau < \pi$
   $R = \dfrac{m\varepsilon_r + 2}{m + \varepsilon_r + 1}$ - ratio of principal polarisabilities
   m — particle shape parameter $m = \begin{cases} >1 & \text{prolate particles} \\ 1 & \text{spherical particles} \\ <1 & \text{oblate particles} \end{cases}$

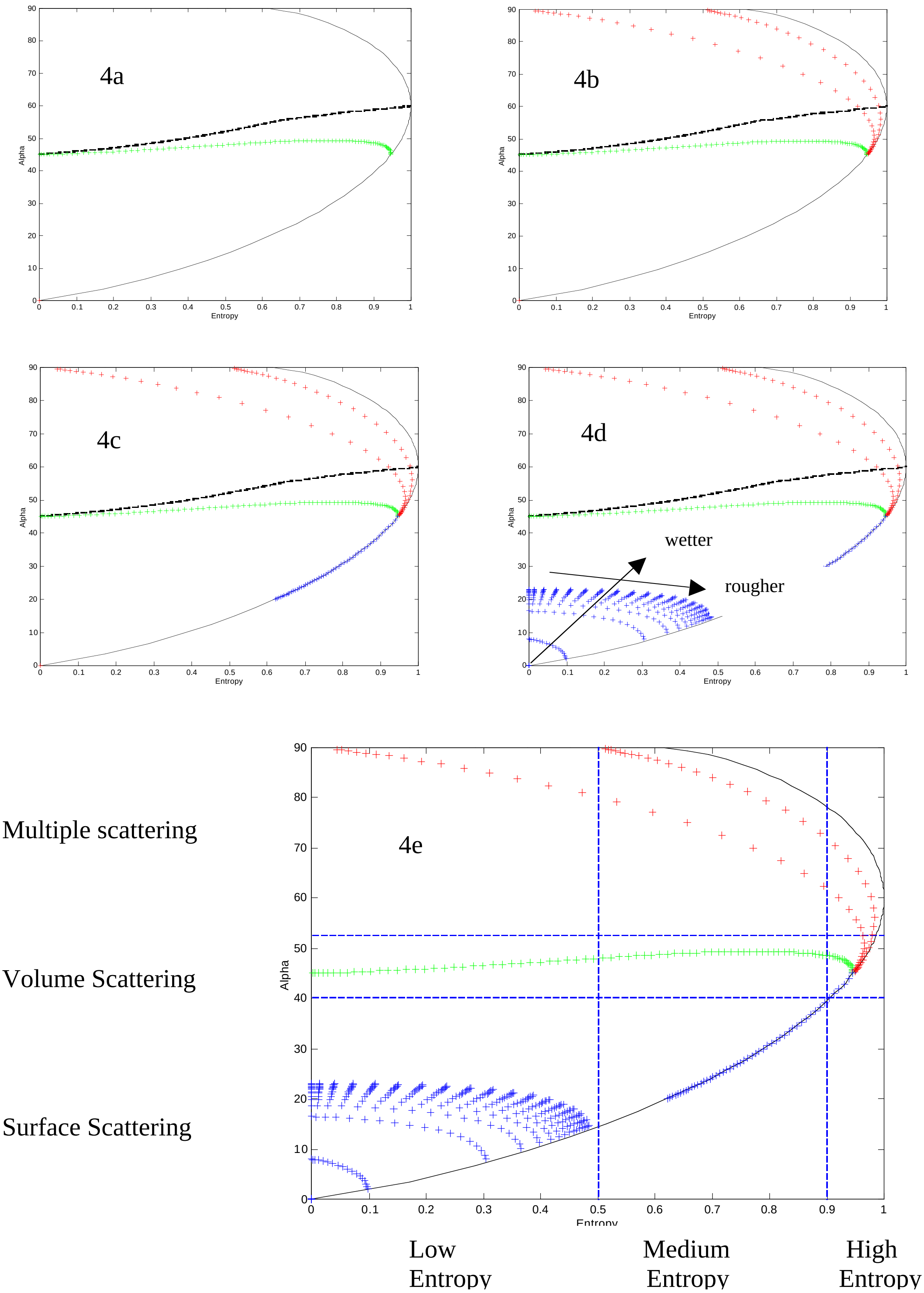

Figure 4 : Segmentation of the H/ α Plane

Extinction E
Leaf (L) + Stalks

Azimuthal Symmetry — uniaxial crystal

$$\boxed{E(\underline{w}) = E_L + E_S(\underline{w})}$$

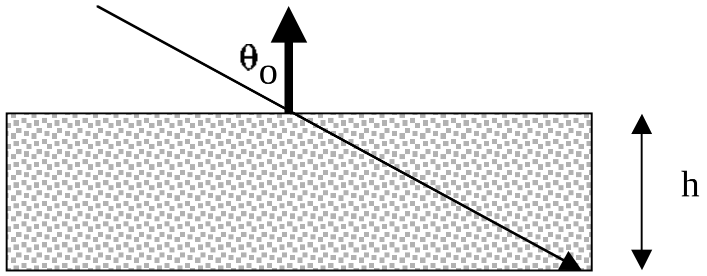

Polarization Dependence

where

$$E_L \approx \exp\left(-\frac{4\pi v_L \varepsilon_L'' h}{3\lambda\cos\theta_o}\right) \Rightarrow h v_L = LAI.\bar{t}$$

$$E_s \Rightarrow \begin{cases} E_{xx} \approx \exp\left(-\frac{4\pi v_L n_o'' h}{\lambda\cos\theta_o}\right) & n_o'' = \mathrm{Im}(\sqrt{\varepsilon_o}) \quad \varepsilon_o \approx (1+2v_s) - i\left(\frac{4 v_s \varepsilon_s''}{(\varepsilon_s'')^2 + (\varepsilon_s')^2}\right) \\ E_{yy} \approx \exp\left(-\frac{4\pi v_L\left(\cos^2\theta_o n_o'' + \sin^2\theta_o n_e''\right)h}{\lambda\cos\theta_o}\right) & n_e'' = \mathrm{Im}(\sqrt{\varepsilon_e}) \quad \varepsilon_e \approx \left(1 + v_s(\varepsilon_s' - 1)\right) - i v_s \varepsilon_s'' \end{cases}$$

Figure 5 : Two component model of vegetation propagation in radar polarimetry

The strongest depolarising effects are caused by extremely prolate particles or dipoles. We can then use equation 8 and the mixed model of figure 5 to generate the H/ α variation of scattering by a cloud of ordered and disordered dipoles. This loci is shown in figure 4a as the green line, which we see lies in the single scattering domain as it should.

Note that when the entropy is zero we have a uniaxial crystal and α is 45 degrees as expected for dipoles. As the volume becomes more random then we see that the entropy increases. However the α value does not vary much, indicating that particle shape is not changing. The limit is obtained for a random distribution, which by definition will lie somewhere on curve I. For completely random distributions [T] is diagonal and the eigenvalues can then be analytically determined from averages of equation 8 as [16,22]

$$\begin{aligned} \lambda_1 &= 2R^2 + 6R + 7 \\ \lambda_2 &= \lambda_3 = (R-1)^2 \end{aligned} \qquad \text{- 9)}$$

For R tending to infinity this yields the highest possible entropy in single scattering from a cloud of particles. This entropy is H = 0.95 and is a key point on the H/α diagram.

Two important problems can now be derived from this H = 0.95 point. The first is to consider the presence of multiple scattering in the volume. This yields the loci shown in red in 4b. The lower locus is for a single multiple scattering component as might arise for example when a dihedral is placed beneath a vegetation canopy. The upper locus is for random effects in the canopy itself when the multiple scattering occurs between randomly oriented particles. We see that as the level of dihedral response increases so these two loci diverge at lower entropy.

The second important problem is to consider variations in particle shape. Although vegetation scattering is generally dominated by prolate objects, some special cases arise when oblate scatterers can be dominant. Using equation 9 we can set R = 0 for a random cloud of oblate scatterers and obtain the minimum entropy as 0.63. Hence a mixed random volume of prolate and oblate particles will lie along the blue loci on curve I as shown in 4c.

Finally we must consider scattering by non-vegetated surfaces. Here an important limiting problem is the Bragg model. This applies in the limit $ks < 0.3$ where k is the wavenumber and s the rms roughness of surface and predicts an entropy H = 0 for all surfaces. The α parameter however is independent of roughness and increases with angle of incidence and with dielectric constant of the surface. The limiting value of α is 45 degrees for grazing incidence when VV is much larger than HH. Hence this model lies along the y-axis of the H/α plane staying in the single scattering regime as it should.

Natural surfaces do not satisfy this model, especially at the important frequency of L-band where many natural roughness scales lie in the range $0.2 < ks < 1$. However, by using a depolarising extension of the Bragg model for rough surfaces it has been shown that the entropy of surface scattering can be non-zero [18]. Figure 4d shows the loci of this model for a surface with increasing roughness and dielectric constant. We note that the maximum entropy increases with angle of incidence but for angles around 45 degrees or less it never exceeds 0.5.

We can now use all these observations to segment the H/α plane into important zones of scattering behaviour. Figure 4e shows a summary of this segmentation with the various model loci superimposed.

Vertically we can distinguish 3 classes of surface volume and multiple scattering. Horizontally we can then segment each into 3 classes of low, medium and high entropy. There results 9 distinct segments although high entropy surface scattering is excluded by the curve I boundary. Hence we obtain 8 useful classes as shown in [1]. Note that these class boundaries are not entirely arbitrary as suggested in [7]. They relate to boundaries between physical models of scattering behaviour. Of course in practice, speckle causes fluctuations in the H/α points and so noisy segmentations. This can be minimised by using a large number of looks in the data or by using this method as the first stage in an iterative statistical classification procedure as demonstrated in [5,7]. Nonetheless it is important to realise that these boundaries are chosen for physical reasons and are not statistical in nature.

To illustrate application of the technique, we show in figure 7 a montage of scenes obtained using the L-band AIRSAR system. On the left we show total power images of the scenes and on the right the corresponding entropy/alpha distributions. In the top image we show a volcanic area, which is a mixture of rough surface and vegetated re-growth areas. The H/α plot shows azimuthal symmetry across this scene and three main classes of terrain cover, namely high entropy volume scattering corresponding to the heavily vegetated areas, medium entropy surface scattering corresponding to rough surfaces and low entropy smoother surfaces. Figure 6 shows the result of an unsupervised classification of these pixels. The color coding is such that 1-2-3 are blue and correspond to surface scattering, 4-5-6 are volume scattering and 7-8-9 multiple scattering.

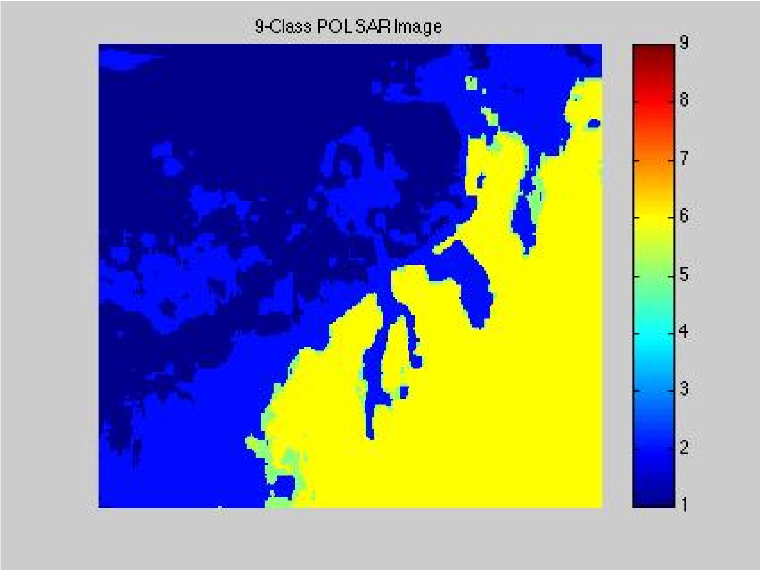

Figure 6 : Unsupervised 9-Class Image of Volcanic Region

In contrast, in the centre of figure 7 we show a tropical forest scene and note a high concentration of pixels in the corresponding high entropy volume scattering class. We notice two clear-cut regions and note from the H/α plots that they have very different polarimetric behaviour, appearing as two distinct tails on the density variations.

Finally, in the lower example we show a sea ice scene. Here we have predominantly surface scattering as expected, although we notice that the scene is not azimuthally symmetric. This is significant as we shall see that it implies that the scattering Anisotropy is an important parameter for sea ice classification.

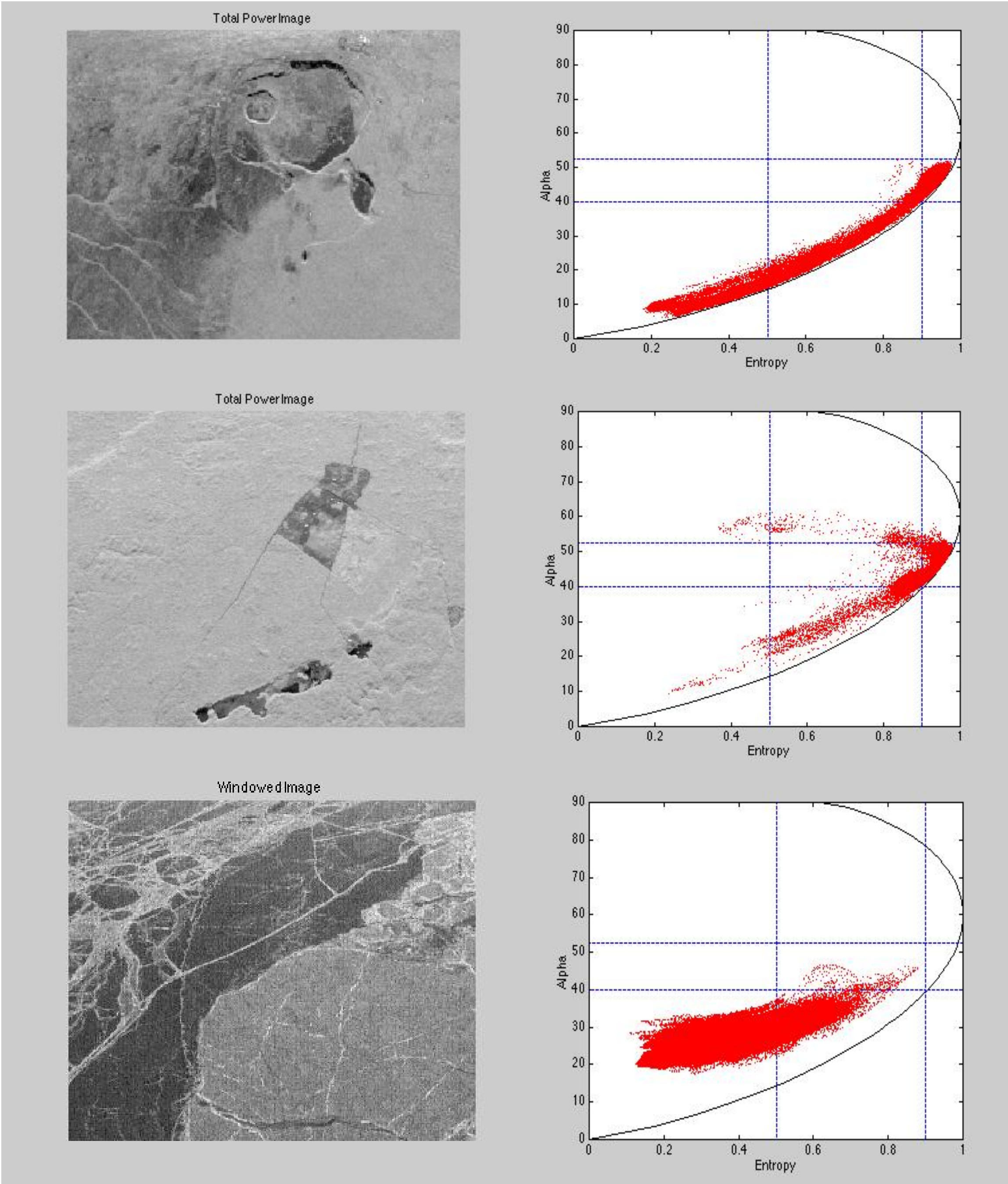

Figure 7 : Montage of H/ α distributions for vegetated lava scene (top), tropical forest (centre) and sea ice (lower)

In order to extend this procedure to more classes, we must first consider features of the polarimetric response not represented by the H/ α plane. We now consider this problem in detail using a general decomposition [13].

3. The Polarising/Depolarising Decomposition

The starting point for our analysis is the idea of point reduction, which states that there exists a cascade of transformations which can be used to reduce any unitary scattering vector to the identity as shown in equation 10

$$\begin{bmatrix} 1 \\ 0 \\ 0 \end{bmatrix} = [R_\alpha]\,[R_\beta]\,[R_\phi]\,\underline{e}_1 = [U_{-1}]\,\underline{e}_1 \qquad \text{- 10)}$$

where the elementary transformations can be written in terms of the scattering vector parameters as shown in equation 11

$$[R_\alpha] = \begin{bmatrix} \cos\alpha & \sin\alpha & 0 \\ -\sin\alpha & \cos\alpha & 0 \\ 0 & 0 & 1 \end{bmatrix} [R_\beta] = \begin{bmatrix} 1 & 0 & 0 \\ 0 & \cos\beta & \sin\beta \\ 0 & -\sin\beta & \cos\beta \end{bmatrix} [R_\phi] = \begin{bmatrix} 1 & 0 & 0 \\ 0 & e^{-i\chi} & 0 \\ 0 & 0 & e^{-i\psi} \end{bmatrix} \qquad \text{- 11)}$$

This allows us to reference the unitary matrix information to the maximum eigenvector, which by definition is the dominant non- depolarizing scattering mechanism. Equation 12 shows how application of the unitary reduction operator to a general N x N unitary matrix leads to an N-1 dimensional representation.

$$[U_{-1}]\,[U_N] = \begin{bmatrix} 1 & \underline{0} \\ \underline{0} & U_{N-1} \end{bmatrix} \qquad \text{- 12)}$$

This is an important result, as it permits factorisation of the eigenvector information into polarizing and depolarizing components as we now demonstrate.

To establish a short hand notation, we employ the following convention to describe partition of the unitary matrix information into polarizing and depolarizing segments. We bracket together the parameters as follows. Inside square brackets we consider only the depolarization effects whereas inside round brackets we consider only polarizing effects

[E+L] depolarizing parameters
(E+L) polarizing parameters

where E is the number of eigenvector parameters and L the number of eigenvalue parameters. Note that the total number of eigenvector parameters = [E] + (E) = dim(SU(N)) — r(SU(N)) where r is the rank of the Cartan sub-algebra or the number of mutually commuting generators [19,20]. On the other hand [L] + (L) = N, the number of non-negative real eigenvalues. We now consider the following special cases of decomposition:

General Bistatic Scattering

In this case [T]/[M] have 16 parameters in total and SU(4) is the governing unitary group which can be decomposed as follows:

SU(4) has dimension 16 and rank 4 so [E]+(E) = 16-4 = 12 and [L] + (L)= 4 . By application of the unitary reduction operator, depolarization in bistatic scattering systems is controlled by [L] = 3 eigenvalues and the SU(3) group for eigenvectors. Now, SU(3) has dimension 8 and rank 2 so that we can write the polarizing/depolarizing decomposition in compact form as

$$[T]_{bistatic} = [6 + 3] + (6 + 1) \qquad - 13)$$

which shows that there are 6 eigenvector parameters associated with depolarization. These can be generated from the Gell-Mann matrices as shown in [19].

Backscatter

In this important special case [T]/[M] have a maximum of 9 parameters and SU(3) is the governing unitary group for the eigenvectors of [T]. This time a significant simplification occurs, as the unitary reduction operator means that all depolarization effects are controlled by SU(2), which has dimension 3 and rank 1. Hence we obtain the important result that in backscatter the polarized/depolarized decomposition can be written in compact form as

$$[T]_{monostatic} = [2 + 2]+(4 + 1) \qquad - 14)$$

which shows that the eigenvectors contain 2 depolarizing parameters, complemented by 2 real eigenvalues. Note that this decomposition makes no assumptions about symmetry (other than reciprocity) and includes the most general case when helicity and arbitrary orientation effects are included. We now turn to consider special cases of equation 14 when symmetry constraints are imposed.

Equation 14 summarises a new decomposition into polarizing and depolarizing components. However, in the remote sensing of random media such as forest and surface scattering, symmetry constraints often further simplify this decomposition [2,19] as we now show.

Azimuthal symmetry

This is the most severe symmetry assumption and leads directly to a diagonal coherency (and Stokes) matrix with 2 degenerate coherency eigenvalues. Consequently, [T]/[M] have only 2 free parameters and the coherency matrix for backscatter can be written as shown in equation 15

$$[T] = \begin{bmatrix} m & 0 & 0 \\ 0 & m\kappa & 0 \\ 0 & 0 & m\kappa \end{bmatrix} \qquad - 15)$$

In this symmetry assumption the polarizing/depolarizing decomposition reduces to equation 16

$$[T]_{az} = [1] + (1) \qquad - 16)$$

In this case only 2 polarization parameters are required to characterize the medium (such as VV power and HH/VV coherence *or* HV but *not* HV and HH/VV coherence as these two are now trivially related). We considered an analytic example of this case in equation 9 for random volume scattering.

This assumption is generally too severe for microwave remote sensing problems of land surfaces and hence we turn to a less restrictive but more practical assumption of reflection symmetry.

Reflection Symmetry

In this case [T]/[M] have 6 free parameters and the coherency matrix can be written as shown in equation 17

$$[T] = [R_{\beta}] \begin{bmatrix} t_{11} & t_{12} & 0 \\ t_{12}^{*} & t_{22} & 0 \\ 0 & 0 & t_{33} \end{bmatrix} [R_{\beta}]^{-1} \qquad - 17)$$

where β is the angle mismatch between radar co-ordinates and the axis of symmetry (for example the local normal in surface scattering). In this case the decomposition has more structure and can be written as shown in equation 18

$$[T]_{ref} = [2] + (4) \qquad - 18)$$

This is a very interesting result as it shows formally that for backscatter from random media with reflection symmetry [E] = 0 and [L] = 2, so the eigenvectors contain *no* information about depolarization but only about the polarizing influence of the dominant eigenvector. All the depolarization information for such media is contained in the 2 minor eigenvalues of [T] and hence can be extracted by using such parameters as the anisotropy or circular LL/RR coherence [3].

4. Extension of the H/α classification technique

In the previous section we detailed a decomposition of general scattering problems into polarising and depolarising components. For backscatter we saw in equation 14 that the polarising component has (4+1) parameters. The single eigenvalue parameter is the amplitude, which we choose to set to unity in this approach. However this still leaves (4) polarising eigenvector parameters. In the original H/α approach we made use of only two of these, namely the alpha and beta angles as shown in figure 3. There are two others, derived from the phase angle between the elements of the scattering vector. We now consider a physical interpretation of each:

The Helicity Phase ψ

This phase is defined in equation 11. We can generate a physical interpretation by generalising equation 8 to include scattering from chiral particles in which case the scattering vector from one such particle can be written as [22]

$$\underline{k} = \begin{bmatrix} 1 & 0 & 0 \\ 0 & \cos 2\theta & -\sin 2\theta \\ 0 & \sin 2\theta & \cos 2\theta \end{bmatrix} \begin{bmatrix} 2+(R-1)\cos^2\tau \\ (R-1)\cos^2\tau \\ i2\kappa(R-1)\cos^2\tau \end{bmatrix} \qquad - 19)$$

where κ is the chiral parameter (+ for left handed and — for right handed particles). Note that this scattering matrix can no longer be diagonalised by a rotation matrix and that the signature of chirality is a 90 degree phase angle between the second and third elements of the scattering vector. This we term the helicity phase as it corresponds to backscatter from a helix as first developed by Krogager and discussed in [2].

We can also generate the eigenvalues of the coherency matrix for a *random* cloud of chiral particles. For small chirality parameter these are given as [22]

$$\begin{aligned} \lambda_1 &= 2R^2 + 6R + 7 \\ \lambda_2 &= (1+4\kappa)(R-1)^2 \\ \lambda_3 &= (1-4\kappa)(R-1)^2 \end{aligned} \qquad - 20)$$

Note how the smallest eigenvalues have now split, generating Anisotropy A. However for chirality this split will be very small and so A will be close to zero, making it very difficult to measure unless the system calibration is very good. More significantly the eigenvectors of the coherency matrix have the form

$$[\underline{e}_1 \quad \underline{e}_2 \quad \underline{e}_3] = \frac{1}{\sqrt{2}} \begin{bmatrix} \sqrt{2} & 0 & 0 \\ 0 & 1 & 1 \\ 0 & i & -i \end{bmatrix} \qquad - 21)$$

This demonstrates that one of the depolarising parameters can also be an indicator of helicity. In the case of equation 21 the dominant eigenvector has zero helicity *but* the presence of chirality in the cloud generates a phase shift in the depolarising subspace.

In conclusion we note that helicity phase can appear in two important parameters;

- In the polarising eigenvector as a phase shift between the second and third elements, or
- In the depolarising subspace as an SU(2) parameter

In the first case we have an ordered arrangement of handed particles while in the latter we have a random cloud. Such handedness can arise naturally in vegetation scattering through the process of *phyllotaxis* [23]. Future studies will address the estimation of these parameters from SAR data

<u>The Propagation Phase χ</u>

Assuming we are working in the eigenpolarization basis then the propagation of a wave can be represented in terms of the two wavenumbers k_a and k_b as

$$\begin{bmatrix} \exp(ik_a z) & 0 \\ 0 & \exp(ik_b z) \end{bmatrix} = \exp(\frac{i(k_a + k_b)}{2} z) \begin{bmatrix} \exp(i\frac{(k_a - k_b)}{2} z) & 0 \\ 0 & \exp(i\frac{(k_a - k_b)}{2} z) \end{bmatrix} \quad \text{- 22)}$$

If we write the differential wavenumber as

$$\upsilon = k_a - k_b$$

then in terms of the two-way path required for radar scattering, we can derive the effect of propagation on the lexicographic scattering vector as a matrix [P] defined as

$$\underline{k}_L(z) = e^{i(k_a + k_b)z} \begin{bmatrix} \exp(\nu z) & 0 & 0 \\ 0 & 1 & 0 \\ 0 & 0 & \exp(-\nu z) \end{bmatrix} \underline{k}_L = P_L \underline{k}_L \quad \text{- 23)}$$

Converting now to the Pauli matrix base so that we can combine rotations with propagation effects, we have

$$P_P = \frac{1}{2}\begin{bmatrix} 1 & 0 & 1 \\ 1 & 0 & -1 \\ 0 & \sqrt{2} & 0 \end{bmatrix} P_L \begin{bmatrix} 1 & 1 & 0 \\ 0 & 0 & \sqrt{2} \\ 1 & -1 & 0 \end{bmatrix} = e^{i(k_a + k_b)z} \begin{bmatrix} \cosh \nu z & \sinh \nu z & 0 \\ \sinh \nu z & \cosh \nu z & 0 \\ 0 & 0 & 1 \end{bmatrix} \quad \text{- 24)}$$

If we now consider only loss-less propagation then the medium become birefringent and displays differential phase shifts between propagating polarization states. In this case P becomes

$$P_P = e^{i\psi} \begin{bmatrix} \cos\mu & i\sin\mu & 0 \\ i\sin\mu & \cos\mu & 0 \\ 0 & 0 & 1 \end{bmatrix} \quad \text{- 25)}$$

This demonstrates that propagation phase appears as a phase shift between the first and second elements of the scattering vector. This is just the angle χ in equation 11. Hence this parameter is an indicator of significant differential phase shifts in the medium. In practice this arises in ordered media when the uniaxial component is significant. It does however contain information on propagation depth and hence on density and height of vegetation, although a better way to access this structural information is through the use of Polarimetric Interferometry [10,11,12,21]

Final consideration must now be given to the depolarising parameters available for backscatter problems. From the eigenvectors we have α and now a helicity phase χ as shown in equation 21. For the eigenvalues, we already make use of the entropy H, but this can be usefully augmented by a second independent parameter, the Anisotropy A.

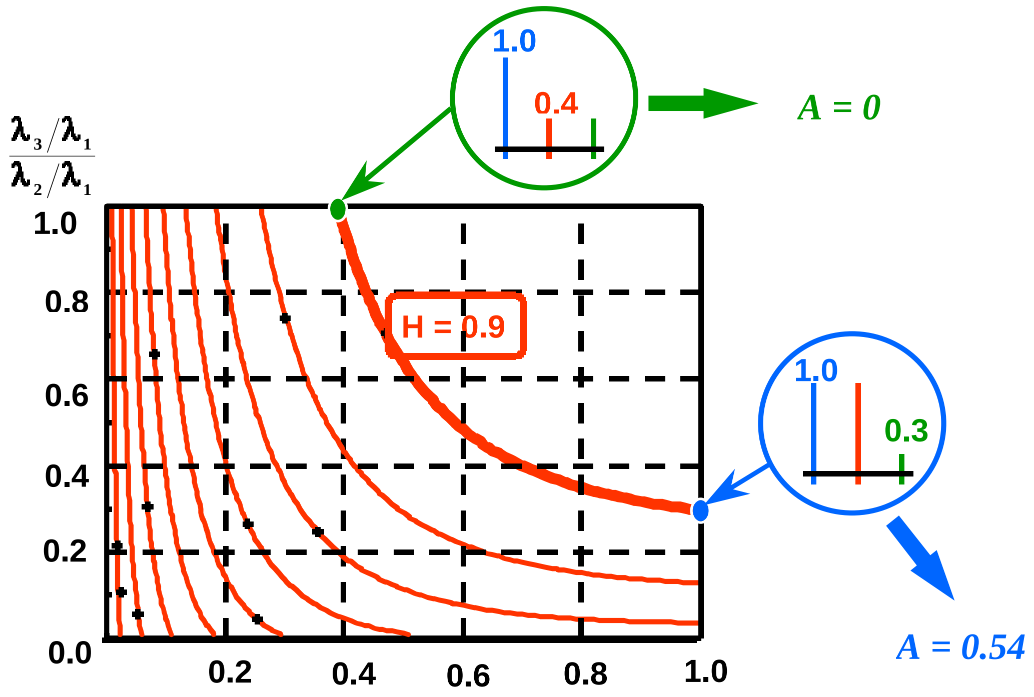

Figure 8 : Anisotropy and Entropy as independent parameters

Figure 8 shows how the same entropy can be obtained for two different anisotropy values. A relates to the ratio of minor eigenvalues of the coherency matrix. We have already seen that azimuthal symmetry forces A = 0 and hence anisotropy can be considered a measure of the departure of the scattering from this severe form of symmetry. The most important class of problems where A becomes significant are those dominated by reflection rather than azimuthal symmetry. In this category there are two important examples, namely scattering by uniaxial particle clouds and scattering by surfaces, where the surface normal is often an axis of symmetry in the problem. In both cases as the system becomes more ordered and less stochastic we can expect a higher anisotropy. Hence A can be used as a measure of surface roughness and of particle orientation distribution [18].

We have already seen an example of this symmetry in surface scattering by sea ice in figure 7. If we apply just the H/α classification then the scene is dominated by 1 class (low entropy surface scattering) as shown on the left of figure 9. However, if we include A then we can see immediately a second important class appear as shown on the right of figure 9. This classification was generated by splitting the data into high and low A segments using a threshold of A=0.5 and then applying the 8 level classification to each segment. The resulting 16 classes are then color coded so that Anisotropy bifurcations are close in the color map. This example demonstrates the importance of using A in initialising the iterative Wishart classifier. Future studies will be extended to include the other parameters in the classification scheme.

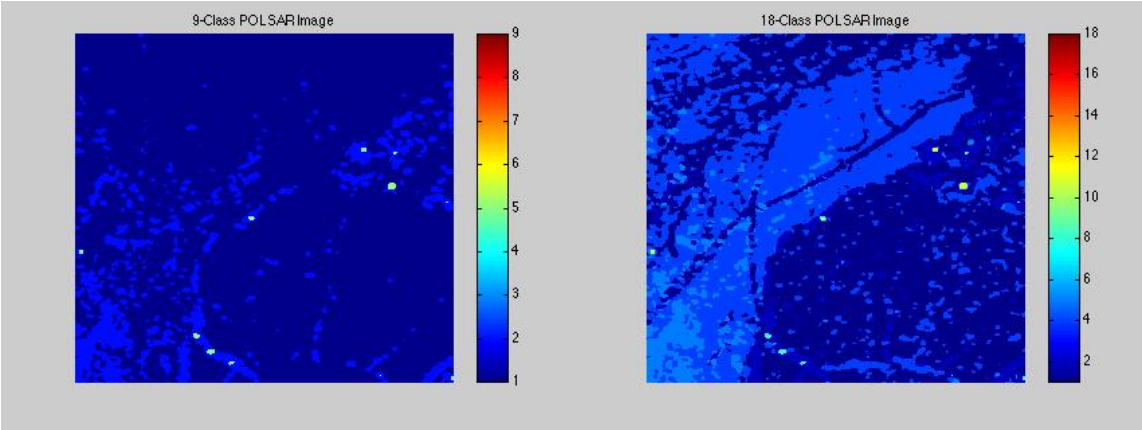

Figure 9 : Sea Ice Classification using H/ α (left) and H/ α/A (right)

5. Conclusions

In this paper we have reviewed the entropy/alpha approach to unsupervised classification of polarimetric SAR imagery. This provides a general purpose, robust method for the classification of a wide diversity of land, sea and ice surfaces. The basic method and its applications have been extensively covered in [1,24]. Here we up-date these papers and extend the original approach using the latest developments in Radar Polarimetry and Interferometry.

We have stressed the role of this technique as the first stage in an iterative maximum likelihood approach based on the Wishart distribution. It follows that it is important to optimise the number and separability of classes at the input of this process. To this end we have presented a full decomposition of scattering problems into polarizing and depolarizing elements. This shows that for backscatter we may have up to 4 new parameters for use in a more refined classifier. Two of these are phase angles from the maximum eigenvector and indicate dominant helicity or propagation phase in the medium. The other two arise from the depolarizing sub-space and can be associated with random chirality and weak propagation effects. Future studies will address the estimation and integration of these parameters into the technique.

We have illustrated the technique with examples from the JPL AIRSAR data base for different types of land cover and have shown that the classification maps so obtained are well correlated with important features in the scene. Such a technique is simple to apply, can be derived from SLC or multi-look Stokes matrix data and provides a natural interface to more elaborate inversion techniques based on detailed physical models.

6. References

[1] S. R. Cloude, E. Pottier, "An Entropy Based Classification Scheme for Land Applications of Polarimetric SAR", IEEE Transactions on Geoscience and Remote Sensing, Vol. 35, No. 1, pp 68-78, January 1997

[2] S. R. Cloude, E. Pottier, "A Review of Target Decomposition Theorems in Radar Polarimetry", IEEE Transactions on Geoscience and Remote Sensing, Vol. 34 No. 2, pp 498-518, March 1996

[3] S R Cloude, K P Papathanassiou, E Pottier,ÓRadar Polarimetry and Polarimetric InterferometryÓ,IEICE Transactions on Electronics, VOL.E84-C, No.12, 2001, pp1814-1822, December 2001

[4] S. R. Cloude, "Physical Realisability of Matrix Operators in Polarimetry", SPIE Vol 1166, Polarization Considerations for Optical Systems II, pp 177-185, August 1989

[5] L. Ferro- Famil, E Pottier and L Jong-Sen, "Unsupervised classification of multifrequency and fully polarimetric SAR images based on the H/A Alpha - wishart classifier", IEEE Transactions - Geoscience and Remote Sensing, Vol 39, Issue 11, November 2001, pp. 2332-2342

[6] J. S. Lee et al, 1994, "Classification of Multi-Look Polarimetric SAR Imagery based on the Complex Wishart Distribution", International Journal of Remote Sensing, Vol. 15(11), pp. 2299-2311

[7] J. S. Lee, M R Grunes, T L Ainsworth, L J Du, D L Schuler, S R Cloude, ÒUnsupervised Classification using Polarimetric Decomposition and the Complex Wishart DistributionÓ,IEEE Transactions Geoscience and Remote Sensing, Vol 37/1, No. 5, p 2249-2259, September 1999

[8] S. R. Cloude, J Fortuny, J M Lopez, A J Sieber, ÒWide Band Polarimetric Radar Inversion Studies for Vegetation LayersÓ,IEEE Transactions on Geoscience and Remote Sensing, Vol 37/2 No 5, pp 2430-2442, September 1999

[9] J. M. Lopez, J Fortuny, S. R. Cloude, A. J. Sieber,ÒIndoor Polarimetric Radar Measurements on Vegetation Samples at L, C, S and X bandsÓ,Journal of Electromagnetic Waves and Applications (JEWA), Vol. 14 No. 2, pp 205-231, February 2000

[10] S. R. Cloude, K. P.Papathanassiou, ÒPolarimetric SAR InterferometryÓ,IEEE Transactions on Geoscience and Remote Sensing, Vol 36. No. 5, pp 1551-1565, September 1998

[11] K.P. Papathanassiou, S. R. Cloude, ÒSingle Baseline Polarimetric SAR InterferometryÓ, IEEE Transactions Geoscience and Remote Sensing, Vol 39/11, pp 2352-2363, November 2001

[12] A. Reigber, K. P. Papathanassiou, S. R. Cloude, A. Moreira, ÒSAR Tomography and Interferometry for the Remote Sensing of Forested TerrainÓ .,Frequenz, 55, March/April, 2001, pp 119-123

[13] S. R. Cloude, ÒA New Method for Characterising Depolarization Effects in Radar and Optical Remote SensingÓ,Proceedings of IEEE International Geoscience and Remote Sensing Symposium (IGARSS 2001), Sydney, Australia, July 2001

[14] S. R. Cloude, ÒPolarimetry in Wave Scattering ApplicationsÓ,Chapter 1.6.2 in SCATTERING, Volume 1,Eds R Pike, PSabatier, Academic Press, 2001, ISBN 0-12-613760-9

[15] Y. Q. Jin, S. R. Cloude, "Numerical Eigenanalysis of the Coherency matrix For a Layer of Random Non-Spherical Scatterers", IEEE Transactions on Geoscience and Remote Sensing , Vol. 32., pp 1179-1185 November 1994

[16] S. R. Cloude, "Uniqueness of Target Decomposition Theorems in Radar Polarimetry", in Direct and Inverse Methods in Radar Polarimetry , Part 1, NATO-ARW, Eds. W.M. Boerner et al, Kluwer Academic Publishers , ISBN 0-7923-1498-0, pp 267-296, 1992

[17] S. R. Cloude, "Vector EM Scattering Theory for Polarimetric SAR Image Interpretation" Chapter 5 in Direct and Inverse Electromagnetic Scattering, Editors , S.R. Cloude, A.H. Serbest, Pitman Research Notes in Mathematics Vol. 361 , Longman Scientific and Technical, pp 217-230, ISBN 0-582-29964-0, 1996

[18] I. Hajnsek, ÒInversion of Surface Parameters using Polarimetric SARÓ,PhD Thesis, Friedrich-Schiller University, Jena, Germany (in English), 2001

[19] S.R. Cloude, " Lie Groups in EM Wave Propagation and Scattering", Chapter 2 in Electromagnetic Symmetry , Eds. C Baum, H N Kritikos, Taylor and Francis, Washington, USA, ISBN 1-56032-321-3, pp 91-142, 1995

[20] S. R. Cloude, "Polarization in Electromagnetic Inverse Problems", Chapter 2 in Inverse Problems and Imaging, Ed. G.F Roach, Pitman Research Notes in Mathematics Vol 245, Longman Scientific and Technical, pp 20-38, 1991

[21] R. N. Treuhaft, S R Cloude,ÒThe Structure of Oriented Vegetation from Polarimetric InterferometryÓ,IEEE Transactions Geoscience and Remote Sensing, Vol 37/2, No. 5, p 2620, September 1999

[22] B. Ablitt, ÒCharacterisation of Particles and their Scattering Effects on Polarized LightÓ, Phd Thesis, University of Nottingham, UK, 2000

[23] ÒSpiral SymmetryÓ,Eds. I Hargittai, C A Pickover, World Scientific, 1992

[24]] W. M. Boerner et al ÒPolarimetry in Remote Sensing: Basic and Applied ConceptsÓ,Chapter 5 in Manual of Remote Sensing, Vol. 8, 3rd edition, F M Henderson, A J Lewis eds. New York, Wiley, 1998